THE METHOD OF FUNDAMENTAL SOLUTIONS FOR BRINKMAN FLOWS. PART II. INTERIOR DOMAINS

ANDREAS KARAGEORGHIS, DANIEL LESNIC, AND LIVIU MARIN

ABSTRACT. In part I, we considered the application of the method of fundamental solutions (MFS) for solving numerically the Brinkman fluid flow in the unbounded porous medium outside obstacles of known or unknown shapes. In this companion paper we consider the corresponding interior problem for the Brinkman flow in a bounded porous medium which contains an unknown rigid inclusion $D \subset \Omega$. The inclusion D is to be identified by a pair of Cauchy data represented by the fluid velocity and traction on the boundary $\partial\Omega$. The fluid velocity and pressure of the incompressible viscous flow in the porous medium $\Omega \backslash \overline{D}$ are approximated by linear combinations of fundamentals solutions for the Brinkman system with sources (*singularities*) placed outside the closure of the solution domain, i.e. in $D \cup (\mathbb{R}^2 \backslash \overline{\Omega})$, assuming, for simplicity, that we analyse planar domains. By further assuming that the unknown obstacle D is star–shaped (with respect to the origin), the inverse problem recasts as the minimization of the nonlinear Tikhonov's regularization functional with respect to the MFS expansion coefficients and the discretised polar radii defining D. This minimization subject to simple bounds on the variables is solved numerically using the MATLAB© optimization toolbox routine `lsqnonlin`.

1. Introduction

The study of viscous fluid flows through porous media is of considerable interest in fields such as petroleum engineering [26] and biological flows [25]. For such systems, the Stokes equations and Darcy's law apply at micro– and macro–levels, respectively, whilst a simple interpolation in between them yields Brinkman's equations, see [10],

$$\Delta \boldsymbol{u} - \frac{1}{\mu} \nabla \mathrm{p} - \kappa^2 \boldsymbol{u} = \boldsymbol{0}\,, \tag{1.1}$$

where $\boldsymbol{u}$ and p are the fluid velocity and pressure, respectively, μ is the dynamic viscosity of the fluid, and $\kappa^2 > 0$ is the resistivity (the reciprocal of permeability) of the porous medium to the flow. For low κ we approach the slow viscous Stokes flow regime, while for large κ we are in the usual Darcy porous medium approximation. In some fluid mechanics applications, the Brinkman equation is an appropriate model for the viscous fluid flow through a cloud of spherical particles [33], random arrays of spheres [27], or small fixed rigid objects [13].

Date: October 11, 2020.

2010 *Mathematics Subject Classification.* Primary 65N35; Secondary 65N21, 65N38.

Key words and phrases. Brinkman flow; method of fundamental solutions; inverse problem; nonlinear minimization.

In the companion paper (Part I), see [17], the method of fundamentals solutions (MFS) [18] with Tikhonov's regularization was developed for solving both direct and inverse problems for the Brinkman flow in the porous medium exterior to an obstacle of known or unknown shape. In the exterior inverse problem which was concerned with the identification of the obstacle, the extra data was the fluid velocity specification/measurement on a curve surrounding the obstacle. In contrast to the exterior inverse problem in an unbounded domain investigated in Part I, the current study deals with the interior obstacle case in a bounded domain in which the Brinkman equation (1.1) and the continuity equation $\nabla\cdot\boldsymbol{u} = 0$ of an incompressible fluid hold in the annular porous medium domain $\Omega\backslash D$ formed in between the unknown obstacle (rigid inclusion), on whose boundary ∂D the no–slip fluid velocity condition $\boldsymbol{u} = \boldsymbol{0}$ holds, and the exterior known boundary $\partial\Omega$ on which both the fluid velocity and traction are specified. Such obstacle identification problems concerning the detection of unknown flaws, faults of defects concealed in a given container using non-destructive testing and solved using the MFS occur not only in porous media but also in electrostatics [7], elasticity [19], thermo-elasticity [22], heat transfer [6] and acoustics [14].

Prior to this work, the centre of mass of D has been reconstructed by means of point sources, disks of fixed size or direct localization of small obstacles, [29]. In the present paper, we investigate the full reconstruction (in terms of size and shape determination) of the obstacle D, assumed star–shaped, by the MFS employed iteratively in the minimization of the nonlinear Tikhonov's regularization functional. In addition, partial boundary data is also considered. A similar method has recently been developed by the authors for the identification of a rigid obstacle immersed in a stationary Oseen fluid flow from boundary measurements, [16].

2. Mathematical formulation

For simplicity, we consider the two–dimensional formulation and analysis of the problem, with the mention that all the development in terms of theory and MFS numerics [21, 23] also holds in three dimensions.

Let $\Omega \subset \mathbb{R}^2$ be a bounded planar simply–connected domain containing an obstacle $D \subset \Omega$ such that $\Omega\backslash D$ is connected. Note that D may actually be formed from the union of several disjoined components, [32, 1, 20]. We assume that the boundaries $\partial\Omega$ and ∂D are sufficiently smooth, e.g. of class C^1. The annular domain $\Omega\backslash D$ is a porous medium through which an incompressible fluid flows so that the Brinkman equation (1.1) holds there, along with the continuity equation

$$\nabla\cdot\boldsymbol{u} = 0 \quad \text{in} \quad \Omega\backslash\overline{D} \quad (\text{where } \overline{D} \text{ denotes the closure of } D). \tag{2.1}$$

The inverse formulation that we are investigating is schematically illustrated in Figure 1. As far as the physical problem is concerned, we model a scenario where an unknown defect, flaw or fault (modelled as a rigid inclusion D) contained in the porous medium Ω is to be detected from Cauchy data fluid (velocity, traction) measurements (2.3) and (2.4) at the boundary of the porous medium container. Similar formulations have previously been considered in the context of stationary Stokes flow of slow incompressible fluids, [2, 3, 8], the Oseen flow, [16], or the full Navier–Stokes equations, [4, 9].

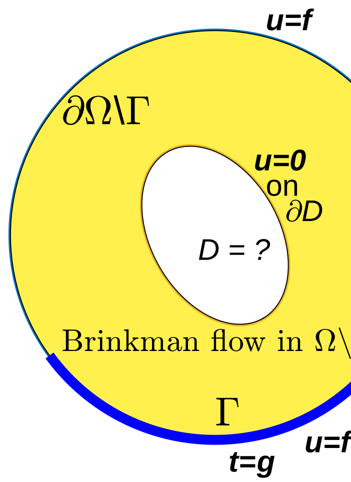

FIGURE 1. Schematics of the inverse problem under investigation

As illustrated in Figure 1, the boundary conditions associated to the partial differential equations (1.1) and (2.1) are:

$$\boldsymbol{u} = \mathbf{0} \quad \text{on} \quad \partial D, \tag{2.2}$$

$$\boldsymbol{u} = \boldsymbol{f} \quad \text{on} \quad \partial\Omega, \tag{2.3}$$

$$\boldsymbol{t} = \boldsymbol{g} \quad \text{on} \quad \Gamma, \tag{2.4}$$

where Γ is a non–empty open portion of $\partial\Omega$ (in many cases $\Gamma = \partial\Omega$), $\boldsymbol{f}$ is a prescribed boundary fluid velocity satisfying

$$\int_{\partial\Omega} \boldsymbol{f} \cdot \boldsymbol{n} \, dS = 0, \tag{2.5}$$

where $\boldsymbol{n}$ is the outward unit normal to the boundary $\partial\Omega$ and $\boldsymbol{g}$ is a prescribed traction (stress force), where

$$\boldsymbol{t} = \left(-p\,\mathbf{I} + \mu\left(\nabla\boldsymbol{u} + (\nabla\boldsymbol{u})^T\right)\right)\boldsymbol{n} \tag{2.6}$$

and $\mathbf{I}$ is the identity tensor. Even more ill–posed formulations consisting of supplying the boundary fluid velocity data (2.3) on Γ instead of the full data over the whole boundary $\partial\Omega$ can also be considered. Assuming that $\boldsymbol{f} \not\equiv \mathbf{0}$, the uniqueness of solution of inverse problem (1.1), (2.1)–(2.4) follows from Holmgren's analytic unique continuation property for the Brinkman (Stokes resolvent) equations [29].

Condition (2.2) represents the usual no-slip condition on a fixed rigid wall that is associated with viscous flow. The inhomogeneous velocity boundary condition (2.3) on $\partial\Omega$ may model a rotating wall condition in case the outer infinitely long cylinder of cross section Ω is rotating.

Another possibility for the inhomogeneous condition (2.3) is to represent an internal fluid velocity measurement in the exterior domain $\mathbb{R}^2 \backslash D$, as previously considered in Part I [17].

3. The method of fundamental solutions (MFS)

The MFS for direct problems of interior Brinkman flows in simply–connected domains was developed in [28, 34]. In this section, we describe the MFS implementation for approximating the velocity $\boldsymbol{u}$ and pressure p satisfying the Brinkman system (1.1) and (2.1) in the multiply–connected domain $\Omega \backslash D$ along with the boundary conditions (2.2)–(2.4). We approximate the fluid velocity $\boldsymbol{u} = (u_1, u_2)$ and pressure p by (note that $\overline{\Omega}$ denotes the closure of Ω)

$$u_i(\boldsymbol{x}) = \sum_{j=1}^{M+N} \left(\alpha_j G_{i1}(\boldsymbol{x}, \boldsymbol{\xi}_j) + \beta_j G_{i2}(\boldsymbol{x}, \boldsymbol{\xi}_j) \right), \quad i = 1, 2, \quad \boldsymbol{x} \in \overline{\Omega} \backslash D, \tag{3.1}$$

$$p(\boldsymbol{x}) = \sum_{j=1}^{M+N} \left(\alpha_j P_1(\boldsymbol{x}, \boldsymbol{\xi}_j) + \beta_j P_2(\boldsymbol{x}, \boldsymbol{\xi}_j) \right), \quad \boldsymbol{x} \in \overline{\Omega} \backslash D, \tag{3.2}$$

where $\left(\boldsymbol{\xi}_j\right)_{j=\overline{1,M+N}}$ are sources located outside the solution domain $\overline{\Omega} \backslash D$ and $\left(G_{ij}\right)_{i,j=1,2}$ and $\left(P_i\right)_{i=1,2}$ represent the fundamental solution of the two–dimensional Brinkman and continuity equations (1.1) and (2.2) given by, see e.g. [31],

$$\begin{aligned} G_{ik}(\boldsymbol{x}, \boldsymbol{x}') = \frac{1}{2\pi\mu\kappa^2 r^2} \Big[&\left(-1 + \kappa r K_1(\kappa r) + \kappa^2 r^2 K_0(\kappa r) \right) \delta_{ik} \\ &+ \frac{(x_i - x_i')(x_k - x_k')}{r^2} \left(2 - \kappa^2 r^2 K_2(\kappa r) \right) \Big], \quad i, k = 1, 2, \end{aligned} \tag{3.3}$$

$$P_k(\boldsymbol{x}, \boldsymbol{x}') = \frac{x_k - x_k'}{2\pi r^2}, \quad k = 1, 2, \tag{3.4}$$

where $\boldsymbol{x} = (x_1, x_2)$, $\boldsymbol{x}' = (x_1', x_2')$, $r = |\boldsymbol{x} - \boldsymbol{x}'|$, $\left(\delta_{ik}\right)_{i,k=1,2}$ is the Kronecker delta tensor, and K_n is the modified Bessel function of the second kind of order n. (Note that throughout the paper, the notation $j = \overline{1, M+N}$ denotes $j = 1, 2, \ldots, M+N$.)

Assuming that, for simplicity, Ω is a disk of radius $R > 0$ centred at the origin and containing the unknown obstacle D (assumed to be star–shaped with respect to the origin) parametrised by

$$\partial D = \left\{ \mathrm{r}(\vartheta) \left(\cos\vartheta, \sin\vartheta \right) | \vartheta \in [0, 2\pi) \right\}, \quad \text{where} \quad 0 < \mathrm{r}(\vartheta) < R, \tag{3.5}$$

the MFS source points $\left(\boldsymbol{\xi}_j\right)_{j=\overline{1,M+N}}$ in expressions (3.1) and (3.2) are taken as

$$\boldsymbol{\xi}_j = \eta_{\text{ext}} \, R \, \left(\cos\vartheta_j, \sin\vartheta_j \right), \quad \vartheta_j = \frac{2\pi(j-1)}{M}, \; j = \overline{1, M}, \tag{3.6}$$

$$\boldsymbol{\xi}_{M+j} = \eta_{\text{int}} \, \mathrm{r}_j \, \left(\cos\tilde{\vartheta}_j, \sin\tilde{\vartheta}_j \right), \quad \tilde{\vartheta}_j = \frac{2\pi(j-1)}{N}, \; j = \overline{1, N}, \tag{3.7}$$

where $\mathrm{r}_j = \mathrm{r}(\tilde{\vartheta}_j)$ for $j = \overline{1, N}$, and $\eta_{\text{ext}} > 1$ and $\eta_{\text{int}} \in (0, 1)$ are dilation and contraction constants which signify that the source points $\boldsymbol{\xi}_j \in \mathbb{R}^2 \backslash \overline{\Omega}$ for $j = \overline{1, M}$ and $\boldsymbol{\xi}_{M+j} \in D$ for $j = \overline{1, N}$. For expressing the stress force (2.6) on $\Gamma \subset \Omega$, we need the normal $\boldsymbol{n} = (n_1, n_2) = (\cos\vartheta, \sin\vartheta)$ and the tensor gradient $\nabla \boldsymbol{u}$, which based on (3.1) and (3.2) yield the MFS approximations for $\boldsymbol{t} = (t_1, t_2)$ given by

$$t_i(\boldsymbol{x}) = \sum_{j=1}^{M+N} \left(\alpha_j D_{i1}(\boldsymbol{x}, \boldsymbol{\xi}_j) + \beta_j D_{i2}(\boldsymbol{x}, \boldsymbol{\xi}_j)\right), \quad i = 1, 2, \quad \boldsymbol{x} \in \Gamma, \tag{3.8}$$

where

$$\begin{aligned}
D_{11} &= -P_1\, n_1 + 2\, \frac{\partial G_{11}}{\partial x_1}\, n_1 + \left(\frac{\partial G_{21}}{\partial x_1} + \frac{\partial G_{11}}{\partial x_2}\right) n_2, \\
D_{12} &= -P_2\, n_1 + 2\, \frac{\partial G_{12}}{\partial x_1}\, n_1 + \left(\frac{\partial G_{22}}{\partial x_1} + \frac{\partial G_{12}}{\partial x_2}\right) n_2, \\
D_{21} &= -P_1\, n_2 + \left(\frac{\partial G_{11}}{\partial x_2} + \frac{\partial G_{21}}{\partial x_1}\right) n_1 + 2\, \frac{\partial G_{21}}{\partial x_2}\, n_2, \\
D_{22} &= -P_2\, n_2 + \left(\frac{\partial G_{12}}{\partial x_2} + \frac{\partial G_{22}}{\partial x_1}\right) n_1 + 2\, \frac{\partial G_{22}}{\partial x_2}\, n_2,
\end{aligned}$$

and the expressions for the partial derivatives $\left(\dfrac{\partial G_{ij}}{\partial x_k}\right)_{i,j,k=1,2}$ are provided in the Appendix.

To apply the boundary conditions (2.2)–(2.4), we select the boundary collocation points

$$\boldsymbol{x}_j = R\,(\cos\vartheta_j, \sin\vartheta_j)\,, \quad j = \overline{1, M}, \quad \text{on } \partial\Omega, \tag{3.9}$$

and

$$\boldsymbol{x}_{M+j} = \mathrm{r}_j \left(\cos\tilde{\vartheta}_j, \sin\tilde{\vartheta}_j\right), \quad j = \overline{1, N}, \quad \text{on } \partial D. \tag{3.10}$$

We also assume, without loss of generality, that Γ contains the first M_1 boundary collocation points $(\boldsymbol{x}_j)_{j=\overline{1,M_1}}$, where $0 < M_1 \leq M$.

Then, the solution of inverse problem (1.1)–(2.4) is sought as a minimizer of the nonlinear Tikhonov–type regularization functional

$$\mathcal{F}(\boldsymbol{\alpha}, \boldsymbol{\beta}, \mathrm{r}, \eta_{\mathrm{int}}, \eta_{\mathrm{ext}}) := ||\boldsymbol{u}||^2_{L^2(\partial D)} + ||\boldsymbol{u} - \boldsymbol{f}||^2_{L^2(\partial\Omega)} + ||\boldsymbol{t} - \boldsymbol{g}^\varepsilon||^2_{L^2(\Gamma)} + \mathcal{R}(\boldsymbol{\alpha}, \boldsymbol{\beta}, \mathrm{r}; \mu_1, \mu_2), \tag{3.11}$$

where $\boldsymbol{\alpha} = (\alpha_j)_{j=\overline{1,M+N}}$, $\boldsymbol{\beta} = (\beta_j)_{j=\overline{1,M+N}}$, noise is introduced in (2.4) as

$$\boldsymbol{g}^\varepsilon = \boldsymbol{g} + \boldsymbol{\varepsilon}, \tag{3.12}$$

where $\boldsymbol{\varepsilon}$ represents the noise, and $\mathcal{R}$ is the regularization term given by

$$\mathcal{R}(\boldsymbol{\alpha}, \boldsymbol{\beta}, \mathrm{r}; \mu_1, \mu_2) = \mu_1\, \left(|\boldsymbol{\alpha}|^2 + |\boldsymbol{\beta}|^2\right) + \mu_2\, ||\mathrm{r}'||^2_{L^2(\partial D)}, \tag{3.13}$$

where μ_1 and μ_2 are positive regularization parameters, which can be prescribed either by trial and error or by using some criterion such as the L-surface method, see [5, 12], or the L–curve method [11, 6] if we take $\mu_1 = \mu_2 = \mu$, or $\mu_1 = 0$ and vary μ_2, or $\mu_2 = 0$ and vary μ_1, see [16].
On discretizing the norms in (3.11) and (3.13), and using the MFS approximations (3.1) and (3.2), we obtain

$$\mathcal{F}(\boldsymbol{\alpha}, \boldsymbol{\beta}, \mathbf{r}, \eta_{\mathrm{int}}, \eta_{\mathrm{ext}}) = T_0 + T_{\boldsymbol{f}} + T_{\boldsymbol{g}^\varepsilon} + \mathcal{R}, \tag{3.14}$$

where $\mathbf{r} = (\mathrm{r}_\ell)_{\ell=\overline{1,N}}$,

$$\mathcal{R}(\boldsymbol{\alpha}, \boldsymbol{\beta}, \mathbf{r}; \mu_1, \mu_2) = \mu_1 \left(|\boldsymbol{\alpha}|^2 + |\boldsymbol{\beta}|^2\right) + \mu_2 \sum_{j=2}^{N} (\mathrm{r}_j - \mathrm{r}_{j-1})^2, \tag{3.15}$$

$$T_0(\boldsymbol{\alpha}, \boldsymbol{\beta}, \mathbf{r}, \eta_{\mathrm{int}}, \eta_{\mathrm{ext}}) = \sum_{i=1}^{2} \sum_{k=1}^{N} \left[\sum_{j=1}^{M+N} \left(\alpha_j G_{i1}(\boldsymbol{x}_{M+k}, \boldsymbol{\xi}_j) + \beta_j G_{i2}(\boldsymbol{x}_{M+k}, \boldsymbol{\xi}_j) \right) \right]^2 \tag{3.16}$$

$$T_{\boldsymbol{f}}(\boldsymbol{\alpha}, \boldsymbol{\beta}, \mathbf{r}, \eta_{\mathrm{int}}, \eta_{\mathrm{ext}}) = \sum_{i=1}^{2} \sum_{k=1}^{M} \left[\sum_{j=1}^{M+N} \left(\alpha_j G_{i1}(\boldsymbol{x}_k, \boldsymbol{\xi}_j) + \beta_j G_{i2}(\boldsymbol{x}_k, \boldsymbol{\xi}_j) \right) - f_i(\boldsymbol{x}_k) \right]^2, \tag{3.17}$$

and

$$T_{\boldsymbol{g}^\varepsilon}(\boldsymbol{\alpha}, \boldsymbol{\beta}, \mathbf{r}, \eta_{\mathrm{int}}, \eta_{\mathrm{ext}}) = \sum_{i=1}^{2} \sum_{k=1}^{M_1} \left[\sum_{j=1}^{M+N} \left(\alpha_j D_{i1}(\boldsymbol{x}_k, \boldsymbol{\xi}_j) + \beta_j D_{i2}(\boldsymbol{x}_k, \boldsymbol{\xi}_j) \right) - g_i^\varepsilon(\boldsymbol{x}_k) \right]^2, \tag{3.18}$$

The regularization term (3.13) (or its discretized version (3.15)) is included in order to stabilize the MFS coefficients $\boldsymbol{\alpha}$ and $\boldsymbol{\beta}$ and impose a H^1-smoothness constraint on the boundary of the obstacle D parameterized through the polar radius $\mathrm{r}(\vartheta)$, as in (3.5), see also the analysis [14] for inverse obstacle acoustic scattering. If we know *a priori* that the sought obstacle is less smooth (possibly having corners) then an L^1-regularization term $\|\mathrm{r}\|_{L^1(\partial D)}$ would be more appropriate in (3.13) instead of the L^2-regularization term $\|\mathrm{r}'\|^2_{L^2(\partial D)}$.
The minimization of functional (3.14) is based on the trust reflection algorithm implemented in the MATLAB© optimization toolbox routine `lsqnonlin` [30]. This is a versatile routine which does not require the gradient of the objective functional to be supplied by the user and, in addition, allows for simple physical bounds on the variables to be prescribed. In our case, the lower and upper bounds are prescribed as

$$-10^5 \le \alpha_j \le 10^5, \quad -10^5 \le \beta_j \le 10^5, \quad j = \overline{1, M+N},$$

$$0 < \mathrm{r}_{\min} \le \mathrm{r}_\ell \le \mathrm{r}_{\max} < R, \quad \ell = \overline{1, N},$$

and

$$0.1 \le \eta_{\mathrm{int}} \le 0.99, \quad 1.1 \le \eta_{\mathrm{ext}} \le 2,$$

where $\mathrm{r}_{\min}$ and $\mathrm{r}_{\max}$ are lower and upper bounds on the size of the obstacle D compactly contained in Ω (assumed to be the disk of radius R centred at the origin).

4. Numerical examples

We take Ω to be the disk of radius $R = 2.5$ centred at the origin and, in general, we consider the case of full traction data (2.4) being supplied, i.e. $\Gamma = \partial\Omega$.
However, limited aperture data (2.4) supplied over an arc $\Gamma \subset \partial\Omega = \partial B(\mathbf{0}; R)$ will also be considered in Example 1 below. For the Brinkman flow we took the parameters $\mu = 1$ and $\kappa = 1$. Numerical experiments carried out in Part I [17] in the case of exterior Brinkman flows revealed that there is no significant change in accuracy of the numerical results when the parameters R, μ and κ are varied.
For the arbitrary star–shaped obstacle (3.5) the additional traction (stress force) data (2.4) is numerically simulated by first solving the direct problem (1.1)–(2.3) with known D using the MFS (with different numbers of degrees of freedom M and N than those employed in the inverse problem to avoid committing an inverse crime).
For the specified fluid velocity (2.3) on $\partial\Omega$ we take, see [2],

$$\boldsymbol{u}(x_1, x_2) = \boldsymbol{f}(x_1, x_2) = (-x_2, x_1), \quad (x_1, x_2) \in \partial\Omega, \tag{4.1}$$

which satisfies the compatibility condition (2.5).
As in (3.12), the stress force data $\boldsymbol{g}$ is perturbed by noise (multiplicative) as

$$\boldsymbol{g}^{\varepsilon}(\boldsymbol{x}_k) = (1 + \chi_k \mathrm{p})\, \boldsymbol{g}(\boldsymbol{x}_k), \quad k = \overline{1, M_1}, \tag{4.2}$$

where $(\chi_k)_{k=\overline{1,M_1}}$ are pseudo–random numbers generated from a uniform distribution in [-1, 1] and p represents the percentage of noise.
In the minimization of (3.14), we impose, in a least–squares sense, a total of $2(M + M_1) + 2N$ equations ($2N$ for boundary condition (2.2), $2M$ for boundary condition (2.3) and $2M_1$ for boundary condition (2.4)) in $2(M+N)+N+2$ unknowns $(\boldsymbol{\alpha}, \boldsymbol{\beta}, \mathbf{r}; \eta_{\text{int}}, \eta_{\text{ext}})$ and we therefore need to take $M_1 \geq 1 + N/2$.
In all the numerical examples considered for the inverse problem we took $N = 20, M = 51$, $M_1 = M \times \text{length}(\Gamma)/\text{length}(\partial\Omega)$, and the initial guesses $\alpha^0 = \beta^0 = \mathbf{0}$, $\eta^0_{\text{int}} = 2/3$ and $\eta^0_{\text{ext}} = 3/2$. Except for the limited aperture case illustrated at the end of Section 4.1, in all numerical simulations we consider only the case of fully specified stress force data (2.4) over the whole of the boundary $\partial\Omega(=\Gamma)$.

4.1. **Example 1: Circular obstacle.** The obstacle D to be reconstructed is a disk of radius

$$\mathrm{r}(\vartheta) = 1, \quad \vartheta \in [0, 2\pi). \tag{4.3}$$

To generate the input stress force data (2.4), the direct problem was solved using the MFS with $M = 60, N = 30, \eta_{\text{int}} = 3/4, \eta_{\text{ext}} = 5/3$ (noting that the accuracy of the numerical results was not significantly affected by any other reasonable choice of $\eta_{\text{int}} \in (0, 1)$ neither too small nor too close to unity and $\eta_{\text{ext}} \in (1, \infty)$ neither too close to unity nor too large).
In the inverse problem we took $\mathrm{r}_{\min} = 0.5$, $\mathrm{r}_{\max} = 1.5$ and the initial guess for the polar radius $\mathbf{r}^0 = \mathbf{0.7}$. For no noise, i.e. $\mathrm{p} = 0$, Figure 2(a) shows the convergence of the numerical reconstructions (obtained by minimizing the unregularized functional (3.14) with $\mu_1 = \mu_2 = 0$) toward the analytical solution (4.3), as the number of iterations `niter` increases.

TABLE 1. Example 1: Maximum absolute errors obtained in the reconstructions presented in Figure 2.

	e	e	e	e
Figure 2(a)	0.300	0.0195	0.0115	0.0082
Figure 2(b)	0.4758	0.1600	0.0871	0.0531
Figure 2(c)	0.4758	0.3413	0.2192	0.0405

Next, the exact data for $\boldsymbol{g}$ is perturbed as in (4.2) using p $= 5\%$ noise. The numerical results obtained with various values of the regularization parameters μ_1 and μ_2 after `niter` =1000 are illustrated in Figures 2(b) and 2(c). From these figures it can be seen that stable and accurate reconstruction are obtained for suitable choices of the regularization parameters μ_1 or μ_2. One can also consider distinct positive regularization parameters $0 < \mu_1 \neq \mu_2 > 0$, but their choice based on the L-surface criterion [5, 12] becomes more tedious.

In order to better quantify the actual error in the reconstructions presented in Figure 2, we also calculated the maximum absolute error in these from

$$e = \max_{\ell=\overline{1,N}} |\mathrm{r}_\ell - 1|,$$

and in Table 1 we present the values of e for each of the cases depicted in the figure.

Next we investigate the limited aperture case when the extra traction data (2.4) is only partially supplied on an arc $\Gamma \subset \partial B(\mathbf{0}; R) = \partial\Omega$ of length 2/3 or 1/3 of the full circumference of the circle $\partial B(\mathbf{0}; R)$.

For p $= 5\%$ noise, the numerical reconstructions when Γ is 2/3 and 1/3 of the exterior circle are presented in Figures 3 and 4, respectively. Although the uniqueness of solution still holds due to the unique continuation principle, we expect the stability and accuracy of the reconstructions to deteriorate as the length of Γ decreases, as less quantitative information is supplied. Consequently, compared to the case of full data (2.4) and $\Gamma = \partial B(\mathbf{0}; R) = \partial\Omega$, illustrated in Figure 2, in the limited aperture case illustrated in Figure 3 for Γ being 2/3 of the exterior circle and Figure 4 for Γ being 1/3 of the exterior circle, the results become more sensitive to the choice of the regularization parameter μ_1 or μ_2 but stable and accurate reconstructions can still be observed.

4.2. **Example 2: Peanut-shaped obstacle.** In this example, we consider reconstructing a more irregular shape than that of the previous example, given by a peanut–shaped obstacle with the parametrisation (3.5) and [15],

$$\mathrm{r}(\vartheta) = \frac{1}{2}\sqrt{1 + 3\cos^2(\vartheta)}, \quad \vartheta \in [0, 2\pi). \tag{4.4}$$

The direct problem was solved with $M = 60, N = 30, \eta_{\text{int}} = 0.825$ and $\eta_{\text{ext}} = 5/3$. In the inverse problem (1.1)–(2.4), we took $\mathrm{r}_{\min} = 0.1$, $\mathrm{r}_{\max} = 1.5$ and the initial guess for the polar radius $\mathbf{r}^0 = \mathbf{1}$. The inputs (4.1) and (4.2) as well as the remaining computational details are the same as

FIGURE 2. Example 1: Reconstructions after `niter` = 1000 iterations for p = 5% noise, (a) with no noise and no regularization, (b) for various values of μ_1 and $\mu_2 = 0$ and (c) for various values of μ_2 and $\mu_1 = 0$.

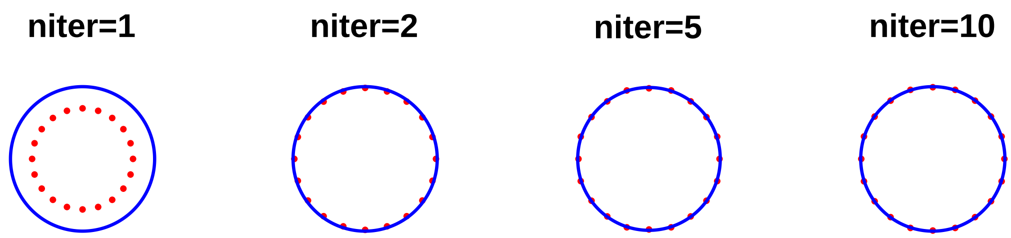

(a)

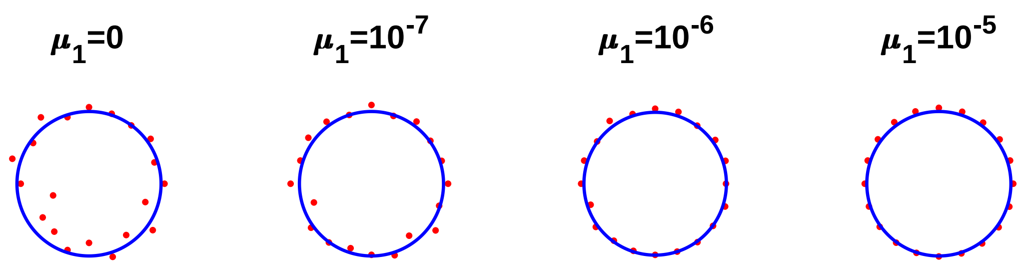

(b)

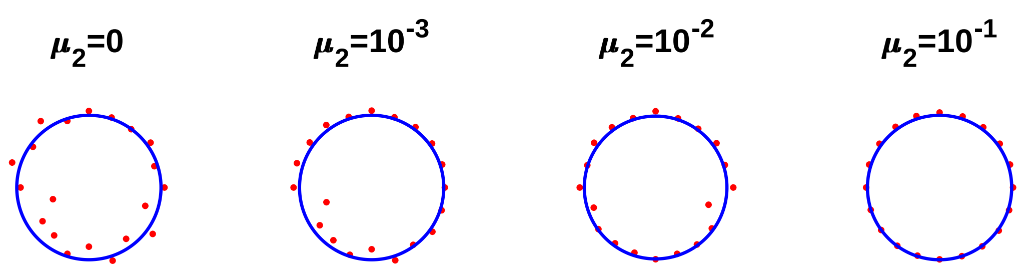

(c)

FIGURE 3. Example 1, aperture case, Γ is $2/3$ of the exterior circle: Reconstructions with p = 5% noise and `niter` = 1000: (a) for various values of μ_1 and $\mu_2 = 0$, and (b) for various values of μ_2 and $\mu_1 = 0$.

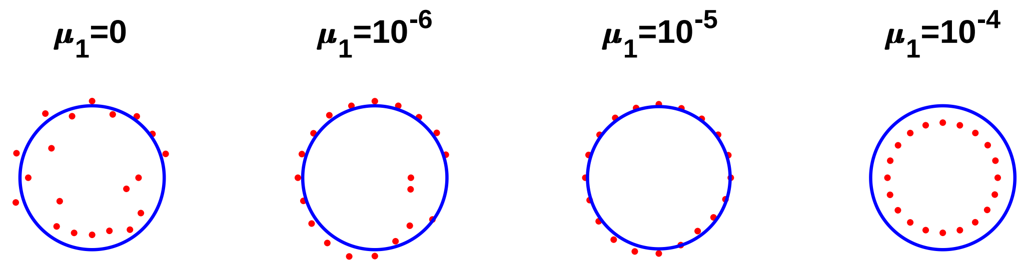

(a)

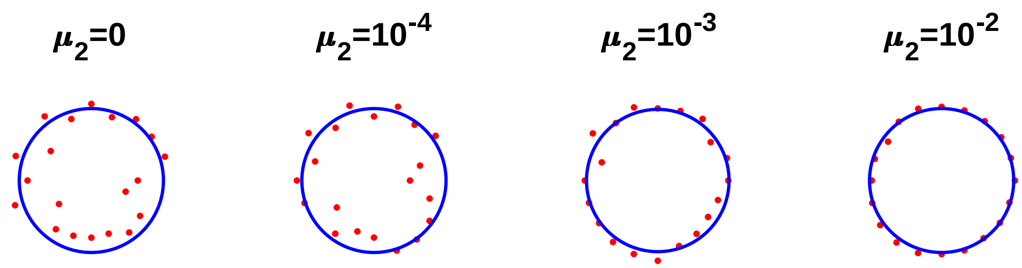

(b)

those in the previous example. Figure 5 represents the same quantities as Figure 2 and the same performant reconstructions in terms of accuracy and stability can be observed.

5. CONCLUSIONS

In this paper, the reconstruction of rigid obstacles immersed in a porous medium through which a Brinkman fluid is flowing has been investigated using boundary fluid velocity and stress force measurements on the exterior fixed boundary. The approximations for the fluid velocity and pressure are based on the MFS linear combinations (3.1) and (3.2) of non–singular fundamental solutions of the Brinkman equations. Further, assuming that the unknown obstacle is star–shaped, the inverse problem has been reduced to a nonlinear minimization problem with respect to the unknown MFS coefficients along with the polar radii parameterising the obstacle. Regularization terms are further added in order to stabilize the solution. The numerical implementation is realized using

FIGURE 4. Example 1, aperture case, Γ is $1/3$ of the exterior circle: Reconstructions with p $= 5\%$ noise and `niter` $= 1000$: (a) for various values of μ_1 and $\mu_2 = 0$, and (b) for various values of μ_2 and $\mu_1 = 0$.

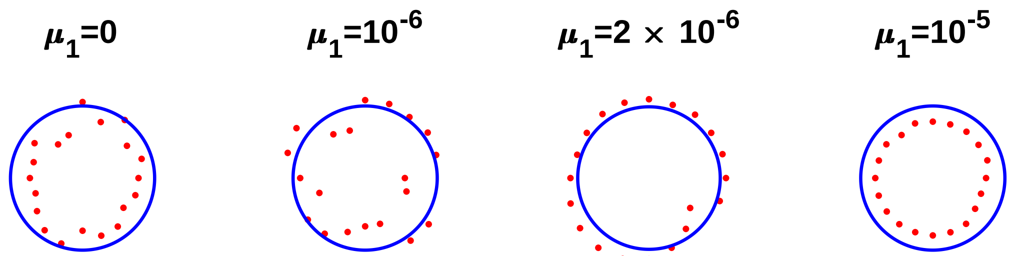

(a)

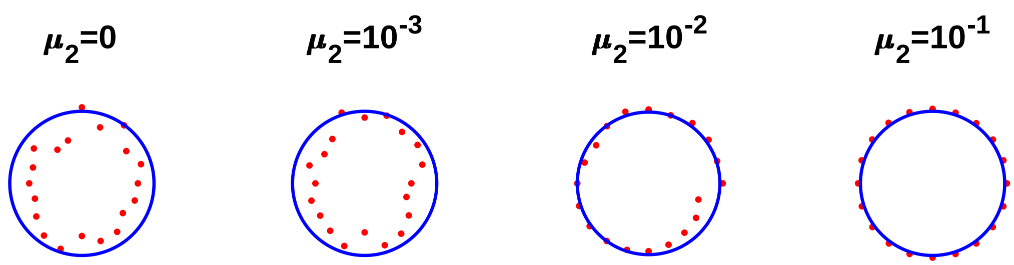

(b)

the MATLAB© optimization toolbox routine `lsqnonlin`. Numerical results have been presented and discussed highlighting the stability and accuracy of the proposed numerical technique. Extensions to the reconstructions of multiple obstacles [20], as well as to three-dimensional Brinkman flows are possible by changing the two-dimensional fundamental solutions (3.3) and (3.4) to their corresponding three-dimensional expressions [34], and using spherical [21, 23] instead of polar coordinates throughout the analysis.

ACKNOWLEDGEMENTS

The authors are grateful to the University of Cyprus for supporting this research.

FIGURE 5. Example 2: Reconstructions (a) with no noise and no regularization, (b) for various values of μ_1 and $\mu_2 = 0$, for p $= 5\%$ noise and `niter` $= 1000$, and (c) for various values of μ_2 and $\mu_1 = 0$, for p $= 5\%$ noise and `niter` $= 1000$.

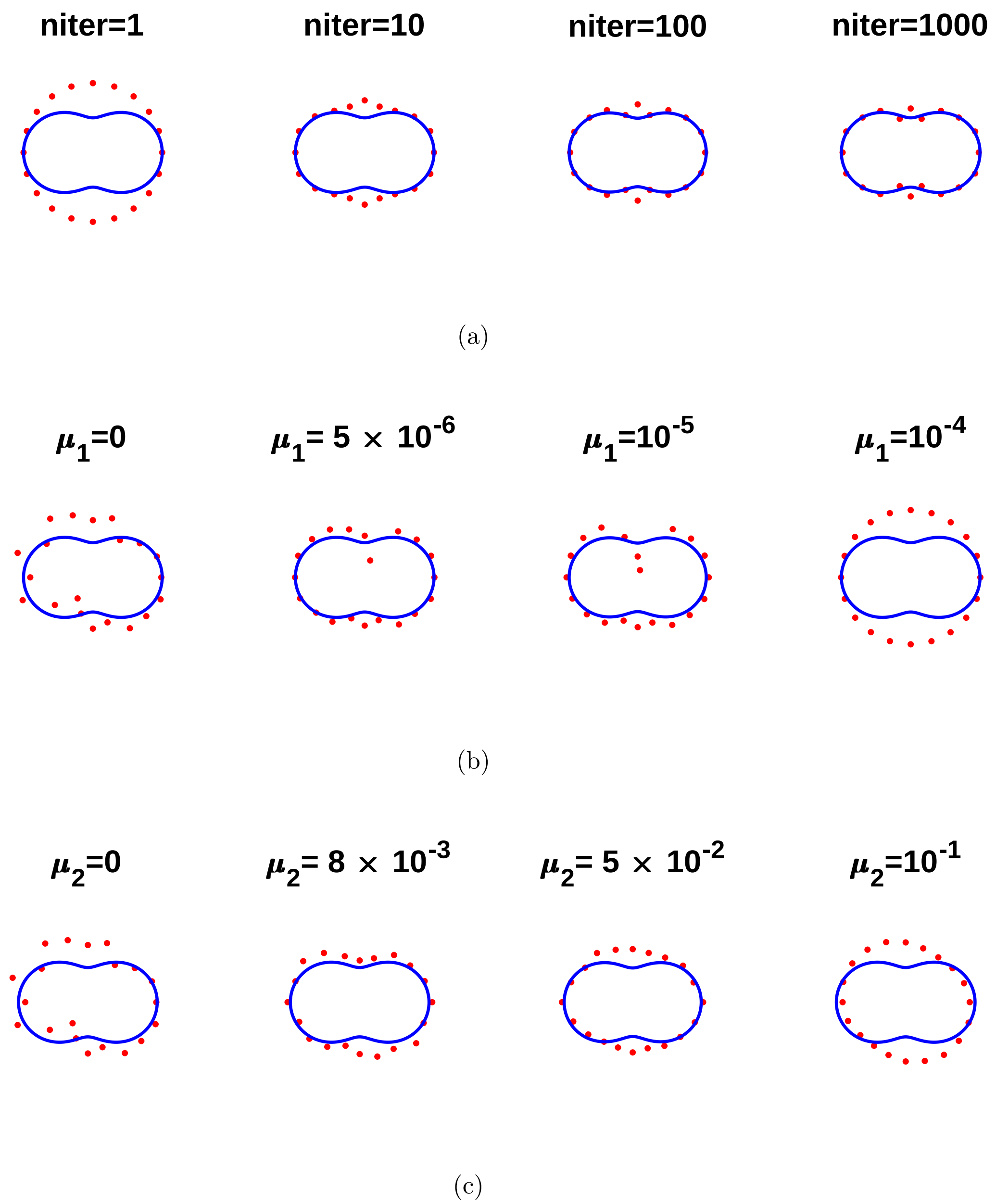

Appendix

In this appendix we provide the expressions for the partial derivatives $\left(\dfrac{\partial G_{ij}}{\partial x_k}\right)_{i,j,k=1,2}$ needed for calculating the matrix $(D_{ij})_{i,j=1,2}$ appearing in the stress force MFS approximation (3.8). First, using the identity

$$\frac{2K_1(z)}{z} = K_2(z) - K_0(z), \quad z \neq 0,$$

we can rewrite (3.3) in the equivalent form, see [24],

$$\begin{aligned} G_{ik}(\boldsymbol{x}, \boldsymbol{x}') = \frac{1}{2\pi\mu} \Bigg[& \left(-\frac{1}{\kappa^2 r^2} + \frac{K_0(\kappa r) + K_2(\kappa r)}{2} \right) \delta_{ik} \\ & + \frac{(x_i - x_i')(x_k - x_k')}{r^2} \left(\frac{2}{\kappa^2 r^2} - K_2(\kappa r) \right) \Bigg], \quad i,k = 1,2. \end{aligned} \tag{A.1}$$

Using that

$$K_0'(s) = -K_1(s), \quad K_2'(s) = -\frac{1}{2}\left(K_1(s) + K_3(s)\right), \tag{A.2}$$

we obtain (checked using the symbolic computation package MAPLE™)

$$\begin{aligned} \frac{\partial G_{11}}{\partial x_1} = \frac{1}{2\pi\mu} \Bigg\{ & \frac{2(x_1 - x_1')}{\kappa^2 r^4} - \frac{\kappa(x_1 - x_1')\left(3K_1(\kappa r) + K_3(\kappa r)\right)}{4r} \\ & + \frac{(x_1 - x_1')^2}{r^2} \left[-\frac{4(x_1 - x_1')}{\kappa^2 r^4} + \frac{\kappa(x_1 - x_1')\left(K_1(\kappa r) + K_3(\kappa r)\right)}{2r} \right] \\ & + \frac{2(x_1 - x_1')(x_2 - x_2')^2}{r^4} \left(\frac{2}{\kappa^2 r^2} - K_2(\kappa r) \right) \Bigg\}, \end{aligned}$$

$$\begin{aligned} \frac{\partial G_{12}}{\partial x_1} = \frac{\partial G_{21}}{\partial x_1} = \frac{1}{2\pi\mu} \Bigg\{ & \frac{(x_1 - x_1')(x_2 - x_2')}{r^2} \left[-\frac{4(x_1 - x_1')}{\kappa^2 r^4} + \frac{\kappa(x_1 - x_1')\left(K_1(\kappa r) + K_3(\kappa r)\right)}{2r} \right] \\ & + \frac{(x_2 - x_2')\left[(x_2 - x_2')^2 - (x_1 - x_1')^2\right]}{r^4} \left(\frac{2}{\kappa^2 r^2} - K_2(\kappa r) \right) \Bigg\}, \end{aligned}$$

$$\begin{aligned} \frac{\partial G_{22}}{\partial x_1} = \frac{1}{2\pi\mu} \Bigg\{ & \frac{2(x_1 - x_1')}{\kappa^2 r^4} - \frac{\kappa(x_1 - x_1')\left(3K_1(\kappa r) + K_3(\kappa r)\right)}{4r} \\ & + \frac{(x_2 - x_2')^2}{r^2} \left[-\frac{4(x_1 - x_1')}{\kappa^2 r^4} + \frac{\kappa(x_1 - x_1')\left(K_1(\kappa r) + K_3(\kappa r)\right)}{2r} \right] \\ & - \frac{2(x_1 - x_1')(x_2 - x_2')^2}{r^4} \left(\frac{2}{\kappa^2 r^2} - K_2(\kappa r) \right) \Bigg\}, \end{aligned}$$

$$\begin{aligned} \frac{\partial G_{11}}{\partial x_2} = \frac{1}{2\pi\mu} \Bigg\{ & \frac{2(x_2 - x_2')}{\kappa^2 r^4} - \frac{\kappa(x_2 - x_2')\left(3K_1(\kappa r) + K_3(\kappa r)\right)}{4r} \\ & + \frac{(x_1 - x_1')^2}{r^2} \left[-\frac{4(x_2 - x_2')}{\kappa^2 r^4} + \frac{\kappa(x_2 - x_2')\left(K_1(\kappa r) + K_3(\kappa r)\right)}{2r} \right] \end{aligned}$$

$$
-\frac{2(x_1-x_1')^2(x_2-x_2')}{r^4}\left(\frac{2}{\kappa^2 r^2}-K_2(\kappa r)\right)\Bigg\},
$$

$$
\frac{\partial G_{12}}{\partial x_2}=\frac{\partial G_{21}}{\partial x_2}=\frac{1}{2\pi\mu}\Bigg\{\frac{(x_1-x_1')(x_2-x_2')}{r^2}\left[-\frac{4(x_2-x_2')}{\kappa^2 r^4}+\frac{\kappa(x_2-x_2')\left(K_1(\kappa r)+K_3(\kappa r)\right)}{2r}\right]
$$

$$
+\frac{(x_1-x_1')\left[(x_1-x_1')^2-(x_2-x_2')^2\right]}{r^4}\left(\frac{2}{\kappa^2 r^2}-K_2(\kappa r)\right)\Bigg\},
$$

$$
\frac{\partial G_{22}}{\partial x_2}=\frac{1}{2\pi\mu}\Bigg\{\frac{2(x_2-x_2')}{\kappa^2 r^4}-\frac{\kappa(x_2-x_2')\left(3K_1(\kappa r)+K_3(\kappa r)\right)}{4r}
$$

$$
+\frac{(x_2-x_2')^2}{r^2}\left[-\frac{4(x_2-x_2')}{\kappa^2 r^4}+\frac{\kappa(x_2-x_2')\left(K_1(\kappa r)+K_3(\kappa r)\right)}{2r}\right]
$$

$$
+\frac{2(x_1-x_1')^2(x_2-x_2')}{r^4}\left(\frac{2}{\kappa^2 r^2}-K_2(\kappa r)\right)\Bigg\}.
$$

References

[1] G. Alessandrini and L. Rondi, *Optimal stability for the inverse problem of multiple cavities*, J. Diff. Equations **176** (2001), 356–386.

[2] C. J. S. Alves, R. Kress and A. L. Silvestre, *Integral equations for an inverse boundary value problem for the two-dimensional Stokes equations*, J. Inverse Ill-Posed Probl. **15** (2007), 461–481.

[3] A. Ballerini, *Stable determination of an immersed body in a stationary Stokes fluid*, Inverse Problems **26** (2010), 125015 (25 pp).

[4] A. Ballerini, *Stable determination of a body immersed in a fluid: the nonlinear stationary case*, Appl. Anal. **92** (2013), 460–481.

[5] M. Belge, M. Kilmer and E. L. Miller, *Efficient determination of multiple regularization parameters in a generalized L-curve framework*, Inverse Problems **18** (2002), 1161–1183.

[6] B. Bin-Mohson and D. Lesnic, *Determination of inner boundaries in modified Helmholtz inverse geometric problems using the method of fundamental solutions*, Math. Comput. Simulation **82** (2012), 1445–1458.

[7] D. Borman, D.B. Ingham, B.T. Johansson and D. Lesnic, *The method of fundamental solutions for detection of cavities in EIT*, J. Integral Equations Appl. **21** (2009), 381–404.

[8] L. Bourgeois and J. Dardé, *The "exterior approach" to solve the inverse obstacle problem for the Stokes system*, Inverse Probl. Imaging **8** (2014), 23–51.

[9] A. Doubova, A. E. Fernández-Cara and J. H. Ortega, *On the identification of a single body immersed in a Navier-Stokes fluid*, European J. Appl. Math. **18** (2007), 57–80.

[10] L. Durlofsky and J. F. Brady, *Analysis of Brinkman equations as a model for flow in porous media*, Phys. Fluids **30** (1987), 3329–3341.

[11] P.C. Hansen, *The L-curve and its use in the numerical treatment of inverse problems*, In: Computational Inverse Problems in Electrocardiology, (ed. P. Johnston), WIT Press, Southampton, pp. 119–142, 2001.

[12] A. Hazanee and D. Lesnic, *Reconstruction of an additive space- and time-dependent heat source*, Eur. J. Comput. Mech. **22** (2013), 304–329.

[13] I. D. Howells, *Drag due to the motion of a Newtonian fluid through a sparse random array of small fixed rigid objects*, J. Fluid Mech. **64** (1974), 449–475.

[14] A. Karageorghis and D. Lesnic, *Application of the MFS to inverse obstacle scattering problems*, Eng. Anal. Boundary Elements **35** (2011), 631–638.

[15] A. Karageorghis and D. Lesnic, *The method of fundamental solutions for the Oseen steady-state viscous flow past obstacles of known or unknown shapes*, Numer. Methods Partial Differential Equations **35** (2019), 2103–2119.

[16] A. Karageorghis and D. Lesnic, *Identification of obstacles immersed in a stationary Oseen fluid via boundary measurements*, Inverse Probl. Sci. Eng. **28** (2020), 950–967.

[17] A. Karageorghis, D. Lesnic and L. Marin, *The method of fundamental solutions for Brinkman flows. Part I. Exterior domains*, submitted.

[18] A. Karageorghis, D. Lesnic and L. Marin, *A survey of applications of the MFS to inverse problems*, Inverse Probl. Sci. Eng. **19** (2011), 309–336.

[19] A. Karageorghis, D. Lesnic and L. Marin, *The method of fundamental solutions for the detection of rigid inclusions and cavities in plane linear elastic bodies*, Comput. Struct. **106-107** (2012), 176–188.

[20] A. Karageorghis, D. Lesnic and L. Marin, *A moving pseudo–boundary method of fundamental solutions for void detection*, Numer. Methods Partial Differential Equations **29** (2013), 953–960.

[21] A. Karageorghis, D. Lesnic and L. Marin, *A moving pseudo–boundary MFS for three-dimensional void detection*, Adv. Appl. Math. Mech. **5** (2013), 510–527.

[22] A. Karageorghis, D. Lesnic and L. Marin, *A moving pseudo–boundary MFS for void detection in two-dimensional thermoelasticity*, Int. J. Mechanical Sciences **88** (2014), 276–288.

[23] A. Karageorghis, D. Lesnic and L. Marin, *The method of fundamental solutions for three-dimensional inverse geometric elasticity problems*, Comput. Struct. **166** (2016), 51–59.

[24] M. Kohr, G. P. R. Sekhar and J. R. Blake, *Green's function of the Brinkman equation in a 2D anisotropic case*, IMA J. Appl. Math. **73** (2008), 374–392.

[25] K. M. Leiderman, L. A. Miller and A. L. Fogelson, *The effect of spatial inhomogeneities on flow through the endothelial surface layer*, J. Theor. Biol. **252** (2008), 313–325.

[26] I. S. Ligaarden, M. Krotkiewski, K. A. Lie, M. Pal and D.W. Schmid, *On the Stokes-Brinkman equations for modelling flow in carbonate reservoirs*, In: Proceedings of the the ECMOR XII - 12th European Conference on the mathematics of Oil Recovery, Oxford, UK, cp-163-00006, 2010.

[27] T.S. Lundgren, *Slow flow through stationary random beds and suspension of spheres*, J. Fluid Mech. **51** (1972), 273–299.

[28] N. F. M. Martins and M. Rebelo, *Meshfree methods for non–homogeneous Brinkman flows*, Comput. Math. Appl. **68** (2014), 872–886.

[29] N. F. M. Martins, *Direct and optimization methods for the localization of obstacles in a porous medium*, In: Engineering Optimization IV, (eds. H. Rodrigues et al.), Taylor & Francis Group, London, pp. 991–996, 2015.

[30] The MathWorks, Inc., 3 Apple Hill Dr., Natick, MA, *Matlab*.

[31] C. Pozrikidis, *Boundary Integral and Singularity Methods for Linearized Viscous Flow*, Cambridge University Press, Cambridge, 1992.

[32] L. Rondi, *Uniqueness and Optimal Stability for the Determination of Multiple Defects by Electrostatic Measurements*, PhD Thesis, University of Trieste.

[33] C. K. W. Tam, *The drag on a cloud of spherical particles in low Reynolds number flow*, J. Fluid Mech. **38** (1969), 537–546.

[34] C. C. Tsai, *Solutions of slow Brinkman flows using the method of fundamental solutions*, Int. J. Numer. Methods Fluids **56** (2008), 927–940.

Department of Mathematics and Statistics, University of Cyprus/ Πανεπιστημιο Κυπρου, P.O.Box 20537, 1678 Nicosia/Λευκωσια, Cyprus/Κυπρος
E-mail address: andreask@ucy.ac.cy

Department of Applied Mathematics, University of Leeds, Leeds LS2 9JT, UK
E-mail address: amt5ld@maths.leeds.ac.uk

Department of Mathematics, Faculty of Mathematics and Computer Science, University of Bucharest, 14 Academiei, 010014 Bucharest, and Institute of Mathematical Statistics and Applied Mathematics, Romanian Academy, 13 Calea 13 Septembrie, 050711 Bucharest, Romania
E-mail address: marin.liviu@gmail.com; liviu.marin@fmi.unibuc.ro